

# Development of a Time-Resolved Energy Absorption Measurement Technique for Laser Beam Spot Welds

*By relating the instantaneous delivered power and pulse energy to the scattered power during welding, a time-resolved description of the power and energy absorption can be obtained*

BY J. T. NORRIS, C. V. ROBINO, M. J. PERRICONE, AND D. A. HIRSCHFELD

## ABSTRACT

A method has been developed to temporally characterize the power and energy absorbed in laser beam spot welding (LBSW). As a spot weld is created, the absorption of laser power changes as the surface of the weld pool changes from initial melting through the development of the keyhole. By relating the instantaneous delivered power and pulse energy to the scattered power during welding, a time-resolved description of the power and energy absorption can be obtained. The method uses two gold-plated integrating spheres containing Nd:YAG notch-filtered photodiodes to capture and detect the scattered laser light. Under various welding parameters (pulse energy, duration, and shape), the level of scattered light changes with the condition of the weld pool. For high

depth-to-width aspect ratio keyhole mode welds, power transfer efficiency (or instantaneous energy transfer) ranges from ~40 to 80% depending on the state of the weld pool. In contrast, low aspect ratio conduction mode welds maintain less than 50% transfer efficiency throughout the welding process. Overall energy transfer efficiencies measured by this method show good agreement with calorimetric (Refs. 1, 2) and thermal expansion measurements (Ref. 4). Time-resolved energy absorption was also evaluated for square and constant ramp down (CRD) pulse shapes. Through characterization of keyhole formation and transfer efficiency in relation to welding parameters, the laser welding process can be optimized, and insight into keyhole phenomena necessary for developing and improving modeling capabilities can be obtained.

energy transfer efficiency to range from 32 to 80% for welds made on titanium Alloy Ti-6Al-4V. In lieu of calorimetry, Cremers et al. determined energy absorption by measuring the thermal expansion of the welded metal sample. The transient displacement of the welded sample was evaluated using interferometry complemented by a second method that monitored coaxial displacement using a linear variable differential transformer (LVDT). Transfer efficiency for this measurement technique ranged from 30 to 62% on 316 SS and 21–50% on Al 1100.

As both calorimetric and thermal expansion measurement techniques correlate well with the average energy transfer determined by the reflections measurement method described here, confidence in this method is established. Development of the reflection measurement method is discussed with emphasis on system calibration and preliminary results that highlight the relevance of temporal mapping to laser process optimization. Total pulse energy transfer and melting efficiency are mapped to reveal the importance of intelligent selection of pulsed laser welding parameters and the effectiveness of pulse shape design.

## Introduction

Power transfer, energy transfer, and melting efficiency are fundamental to the welding process. Mapping these efficiencies to process parameters allows process optimization (Refs. 1–3, 6). With the finer resolution provided by temporal measurements, a better understanding of such phenomena as keyhole formation and laser beam interactions may be obtained. The measurement technique presented here determines the power and energy transfer to the part by evaluating the difference between two independent temporal measurements: one of the delivered laser power and one of the power reflected during welding. Fueschbach et al. (Ref. 1) characterized pulsed laser weld energy absorption through

calorimetry by using hundreds of spot-on-plate welds made in rapid succession on 304 stainless steel. As the welds cooled to room temperature, the energy released was measured by a calorimeter. These results were then divided by the number of welds to yield the average energy absorbed per weld. The energy absorbed was found to range from 38 to 67% of the delivered pulse energy. Temporal resolution is not obtained by this method, and for low-pulse-energy welds, absorption measurements can be difficult.

Micro-calorimetry was performed by Perret et al. (Ref. 2). Perret measured en-

## Experimental Procedures and Calibrations

### Integrating Sphere Configuration

An integrating sphere is an optical device that is hollow and spherical in shape. The interior is coated for a specific light source wavelength to maximize transmittance and promote lambertian reflectance. The result, ideally, is isotropic illumination of the sphere's interior walls (Refs. 4–6). An aperture on the side of the sphere allows a flux of constant irradiance light to be measured with a photodiode that is optically filtered to isolate the desired wavelength(s). The current method for time-resolved energy absorption uses two gold-plated integrating spheres. A schematic of this setup is presented in Fig. 1. In this approach, the

## KEYWORDS

Laser Beam Welding  
Stainless Steels  
Process Control/Monitoring  
Process Optimization  
Keyhole Mode Welds

J. T. NORRIS (jjnorr@q.com) and C. V. ROBINO are with Sandia National Laboratories, Albuquerque, N.Mex. M. J. PERRICONE was formerly with Sandia National Laboratories but is currently with R. J. Lee Group, Monroeville, Pa. D. A. HIRSCHFELD is with New Mexico Institute of Mining and Technology, Socorro, N.Mex.

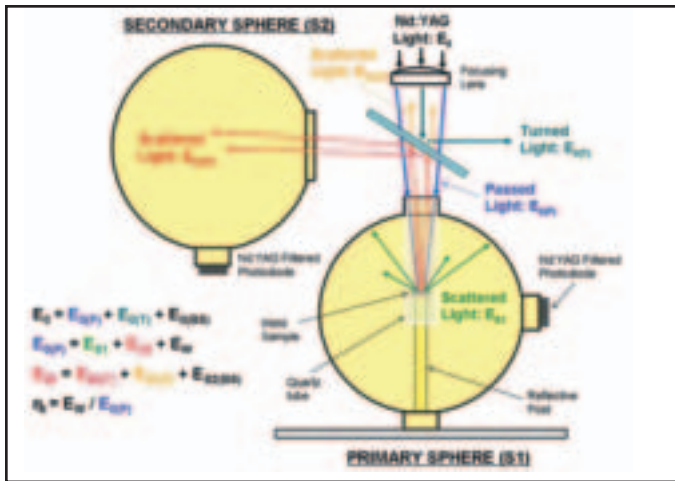


Fig. 1 — Schematic of energy absorption setup including energy balance. Energy absorbed by the weld and beam splitter are denoted with subscripts W and BS, respectively. Subscripts P and T indicate energy that passed through and was turned by the beam splitter.

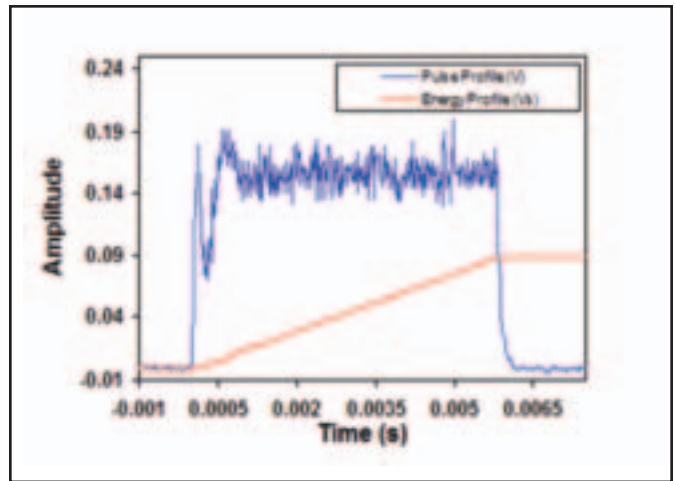


Fig. 2 — Typical waveform captured with an integrating sphere and photodiode.

total scattered energy collected by the two spheres is subtracted from the known delivered laser pulse energy to determine the absorbed energy. The two gold-plated integrating spheres contain a narrow band-pass filtered photodiode to measure light flux as a function of time. A beam splitter is used to redirect possible exiting reflections from the weld sphere into the secondary sphere. The first (or primary) sphere is positioned directly beneath the fiber delivery laser head assembly (source light). The weld sample (here, a 304L stainless steel 12.5-mm-diameter disk, 3 mm thick with a surface finish of  $\sim 0.8 \mu\text{m RMS}$ ) is contained within the sphere and is positioned at sharp focus by an adjustable gold-plated post. Depending upon the state of the weld pool (initial melting  $\rightarrow$  conduction  $\rightarrow$  keyhole), the reflected light from the weld's surface is either captured by the weld sphere or exits through the sphere's 25-mm entrance opening and is captured by the secondary sphere. [Preliminary tests revealed a secondary sphere to be necessary due to the entrance angle of the primary sphere and the beam focus angle forcing focused welds to be conducted above the centerline of the primary

sphere rather than at the more optimal base of the sphere. Thus, a significant amount of the reflected light was found to escape from the entrance hole of the primary sphere, and in order to account for this loss, the secondary sphere was added to collect this light. This will be discussed later in further detail.] The captured light is integrated within each respective sphere, filtered by a  $1064 \pm 3\text{-nm}$  wavelength narrow band-pass filter, and then measured with an InGaAs photodiode with a variable resistance terminator (VRT) and a LeCroy Waverunner oscilloscope. The VRT allows for quick adjustment of the voltage output for optimal signal resolution from the photodiode. The result is a temporally defined voltage that varies in amplitude with light intensity.

A sample of the exiting laser reflections are redirected with a 70:30 ratio beam splitter. The beam splitter is optically coated for a 45-deg maximum transmittance angle and mounted accordingly in the vertical path of the exiting light. Only a 30% sample of the reflected light is directed to the secondary sphere; the remaining 70% continues toward the laser head. As the beam splitter is positioned to

redirect a sample of all exiting reflections, it also redirects a fraction of the incoming focusing laser light ( $E_{0(T)}$ ) — Fig. 1. This fraction is discarded, but by measuring the delivered pulse energy at a position coinciding with the workpiece location (after the beam splitter), it has no effect on the system's calibration. To accurately quantify the scattered laser light during welding, system calibration is paramount. Calibration, design of the sample positioning post, and the effect of the quartz tube weld shield (Fig. 1) are discussed in detail later.

### Primary Sphere Calibration

Temporal pulse characterization provides an accurate description of the pulse generated by the laser for a specific laser setting. The amplitude of the waveform in volts is scalable to the laser's output power. Stability of the laser, which is characterized by consistent energy distribution over time, is determined by comparison of multiple measurements of a set parameter. The pulse-forming capability of the laser may also be verified through this method. In Fig. 2, a typical temporal profile for a square (or top-hat) pulse of 6 ms (blue curve) is presented. The initial fluctuation in output about the nominal at the start of the pulse is common for modern processing lasers of this type, as are the several microsecond ramp-up and -down times. After approximately 1 ms, a nominal output is reached with only moderate jitter in the light intensity detected. Since the output of the photodiode prior to the laser pulse does not show similar fluctuations, this scatter is not considered noise but is either a lack of total light integration within the sphere or real variation in energy output from the laser. Either assumption is adequate for this study. The red curve is an integration of the pulse

Table 1 — Secondary Sphere Energy Distribution Data

Pulse Length (ms)	Pulse Energy (J)	Sphere I (uVs)	Sphere II (uVs)	Energy in Sphere I (J)	Energy in Sphere II (J)
6	1.40	26	446	0.27	1.13
6	0.64	14	205	0.15	0.49
4	0.31	9	101	0.09	0.22
4	0.73	16	223	0.17	0.56
4	1.15	26	358	0.27	0.88
4	1.60	35	489	0.37	1.23
4	2.00	47	616	0.49	1.51
4	3.00	68	920	0.71	2.29

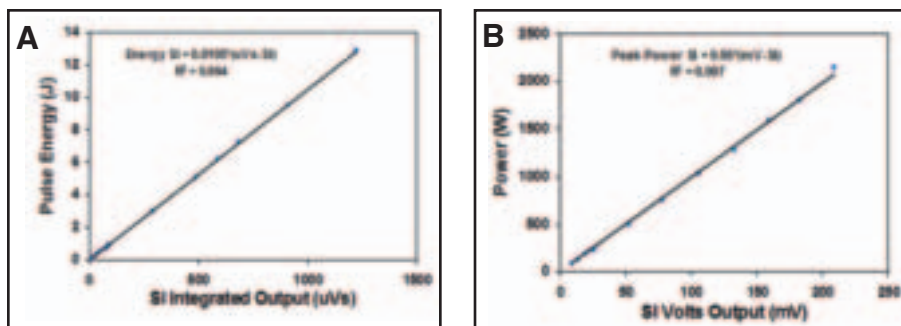


Fig. 3 — Primary sphere calibration profiles for pulse energy: A —  $E_{0(P)}$ ; and B — power.

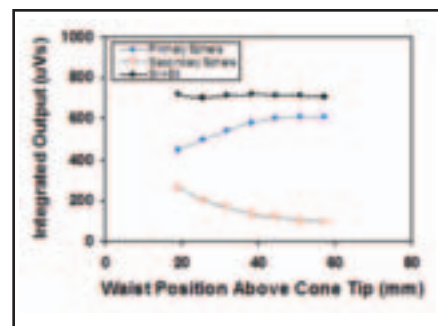


Fig. 4 — Laser beam waist effect on photodiode output.

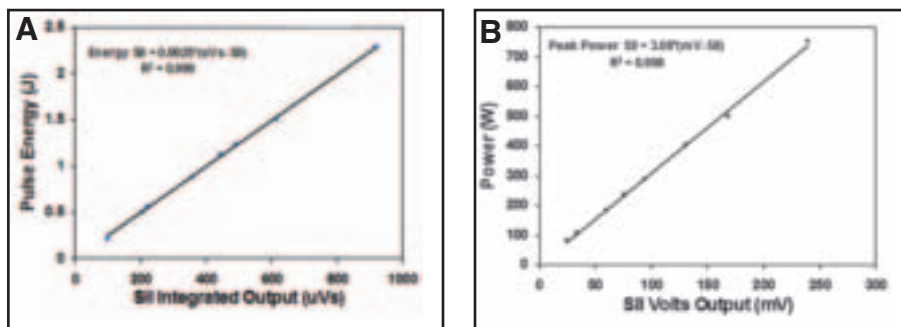


Fig. 5 — Secondary sphere calibration profiles for pulse energy: A —  $E_{0(P)}$ ; and B — power.

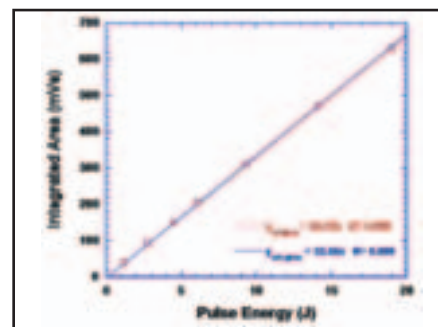


Fig. 6 — Energy mapping with (red) and without (blue) quartz weld shield.

waveform (volts\*seconds) and can be correlated to the energy pulse ( $E_{0(P)}$ ). By independently measuring the pulse energy at the workpiece (an Ophir L40 energy meter was used here), the amplitudes of both waveforms (volts and volt\*seconds) are calibrated to the nominal power and delivered energy ( $E_{0(P)}$ ), respectively, of the laser pulse. Nominal power is calculated as follows:

$$Power = \frac{Pulse\ Energy\ (Joules)}{Pulse\ Time\ (seconds)} = \frac{E_{0(P)}}{t_p}$$

Mapping a series of processing parameters of various power and energy, respectively, yields the necessary calibration equations for power to voltage ( $Power = 9.95 * millivolts$ ) and energy to volt\*seconds ( $Energy = 0.0105 * microvolt-seconds$ ). Calibration of the primary sphere is presented in Fig. 3.

#### Effect of Weld Sample Position

A pulse profile, or waveform, is captured by targeting a defocused beam onto a reflective cone inside the integrating sphere. By placing the cone at the base of the sphere, direct reflections off the cone, which can possibly damage or saturate the photodetector, are avoided. The result is a measure of only integrated reflected laser light. Ideally, weld trials would also be conducted at the base location. However, due to the sphere's 25-mm opening, the raw beam size, and the divergence of the

150-mm focal length lens, focused welds at this location could not be made without clipping the beam. As a result, a gold-plated positioning post and a reflective cone were designed to place the sample at a height sufficient for focused welding. Welding and calibration were conducted at the same height to ensure consistency between welding and calibration. A weld sample height of 15 mm above the sphere's center was chosen, preferentially directing reflections to the upper half of the sphere and preventing direct exposure of the photodiode detector.

During calibration of the primary sphere and diode system, it was found that the photodetector's output varied with the size of the laser beam illuminating the cone. As the cone's tip is not infinitely sharp, a small spot size nearing focus will effectively encounter a flat reflective plate as opposed to a sharp pointed cone. The result is more light reflected into the secondary sphere and less light retained in the primary — Fig. 4. The sum of the reflected light measured by each sphere is constant (black curve) regardless of spot size. For calibration of the primary sphere, it is desired to minimize exiting reflection as the measured pulse energy taken at the workpiece is scaled to the volt\*seconds output of the primary sphere. A large defocused beam is therefore preferred during calibration. The maximum output produced by the diode for a fixed weld schedule was observed when the beam nearly filled the diameter of the cone. This

occurred when the laser was focused 45 mm above the cone's tip.

#### Secondary Sphere Calibration

As the calibration of the primary sphere was carried out by relating the diode's output to the measured pulse energy ( $E_{0(P)}$ ), a similar approach was taken to calibrate the secondary sphere. By substituting the gold cone that was previously used to calibrate the primary sphere with a gold reflective plate (positioned orthogonal to the beam), laser light is split, redirecting most of the light, but not all, to the secondary sphere. By applying the primary sphere's energy calibration, any retained light within the primary sphere is quantified; thus, the energy exiting the sphere can be calculated,  $E_{0(P)} - E_{S-I} = E_{S-II}$  (Table 1). This quantity of energy is used to scale the volts\*seconds output of the secondary sphere. Repetition of this process at various pulse energies yields a calibration of the secondary sphere. By this approach, characterization of energy loss through the 70/30 beam splitter and the distribution of turned and passed energy to the total redirected energy is rendered unnecessary. Instead, with this approach a direct calibration is obtained. Energy and power calibration for the secondary sphere are presented in Fig. 5.

#### Effects of Quartz Weld Shield

To avoid damage or contamination while

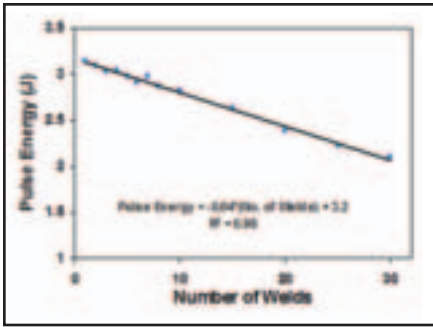


Fig. 7 — Metal vapor deposition on weld shield.

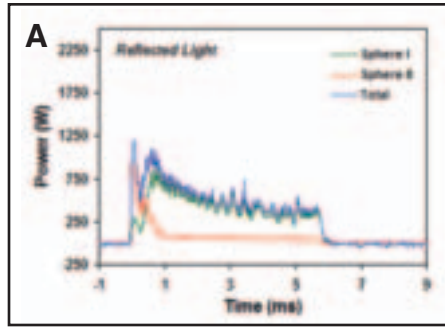


Fig. 8 — A — Reflections measurement; and B — micrograph for keyhole mode weld (6 ms, 9.5 J).

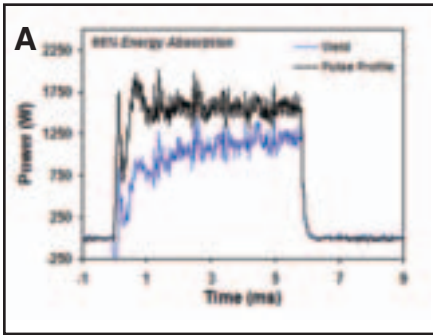


Fig. 9 — Comparison of delivered (black) and absorbed (blue) power for the following pulse shapes: A — square; and B — CRD.

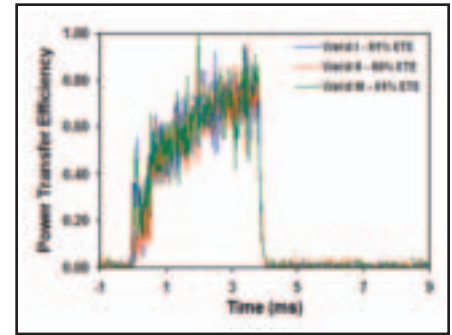


Fig. 10 — Three replicate square pulse spot welds of 4 ms and 6.2 J.

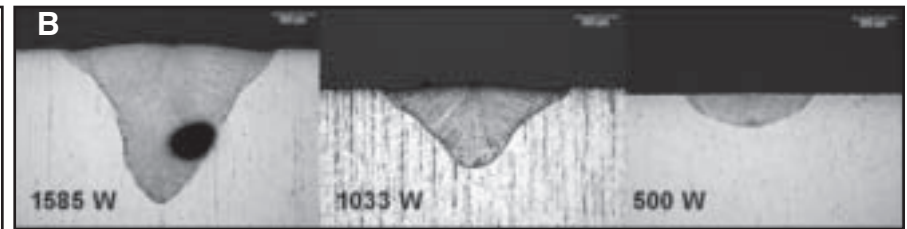
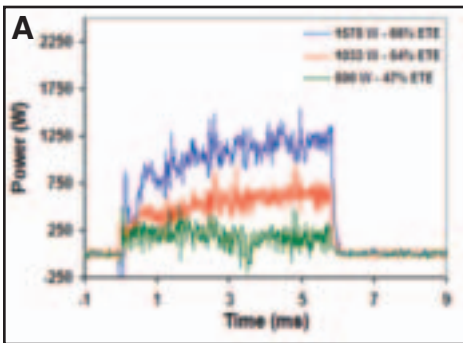


Fig. 11 — A — Evaluation of increased power for 6-ms welds; and B — corresponding metallographic cross sections.

welding inside the gold-plated sphere, a quartz weld shield (a cylinder of fused silica) was positioned from the top of the sphere down to the weld sample — Fig. 1. Without shielding, continued buildup of metal vapor on the sphere's interior would absorb reflections from the weld yielding an artificially high measure of weld energy absorption. To quantify the effect of the weld shield on the 1064-nm Nd:YAG wavelength, temporal profiles were made by characterizing pulse energy vs. volt\*seconds with and without the shield in place. A range of processing parameters of varying pulse energy were examined. Figure 6 shows two overlaying curves demonstrating the weld shield to be transparent (under these conditions) to the Nd:YAG wavelength.

The effect of metal vapor deposition on the shield was also evaluated. Multiple welds were made without any removal of the accumulated metal vapor (on the shield's interior) noting the effect on the resulting measured pulse energy. This test

was run at 6 ms, 9.5 J. As metal vapor accumulated with each weld, lower pulse energies were measured — Fig. 7. The condensed metal layer absorbs an increasing fraction of the reflected light, reducing the amount detected by the photodiode. For a 20-mm-diameter shield and 1575-W peak power, about a 0.04-W energy loss occurred for each additional weld. As power and energy are changed, the rate of metal vaporization and the rate of metal deposition are also changed. While this test only characterizes the specified weld schedule, it is nevertheless indicative of the effect of an increasingly contaminated shield. To avoid metal vapor buildup, the quartz shield was replaced or cleaned (typically with an isopropyl alcohol cloth) between each weld test.

#### Welding Parameters

This study utilized a Lasag SLS C16 fiber-delivered, 40-W average power

pulsed Nd:YAG laser beam welding machine. Focused spot-on-plate welds were produced with a 150-mm focal length lens. Beam characterization below the beam splitter was carried out via Kapton film (Ref. 8) to identify the beam's waist location. This enabled weld trials to be conducted at sharp focus to optimize keyhole mode welding. Preliminary trials included pulse lengths from 2 to 8 ms with pulse energies from 1.5 to 13 J; pulse energy was measured using an Ophir L40(150)A energy meter. Delivered power varied from 500 to 1600 W. Welds were shielded by using UHP argon. Both square and constant ramp down (CRD) pulse shapes were evaluated; a CRD pulse starts at a high output power and decreases linearly to zero to complete the pulse.

#### Results and Discussion

Presented in Fig. 8 is the measured reflected light for a 6-ms, 1575-W peak power

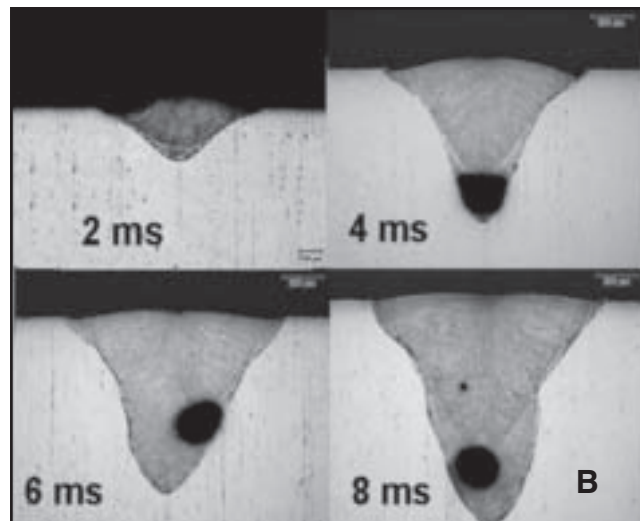
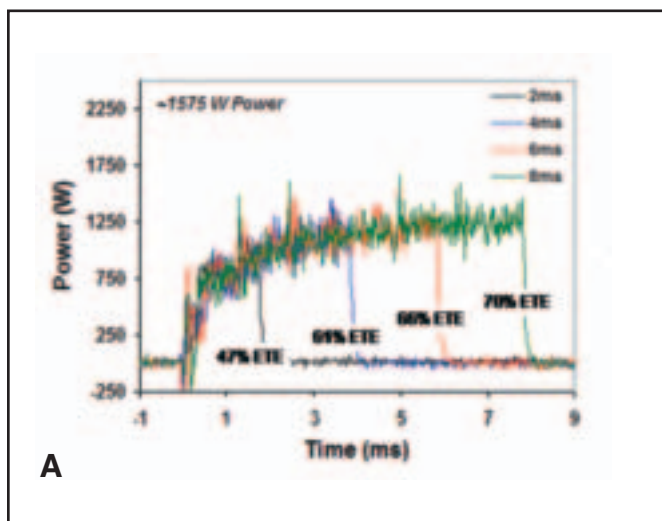


Fig. 12 — A — Evaluation of increasing pulse time for 1575-W welds; and B — corresponding metallographic cross sections.

pulse (~9.5 J/pulse). The green and red curves represent the reflected Nd:YAG light detected by the primary and secondary spheres, respectively. The appropriate voltage-to-power calibrations were applied to yield a plot of power vs. time, and the area under the curve corresponds to the reflected energy. The sum of the two profiles is depicted by the blue curve, and represents the overall power reflected off the weld at each point in time. By comparing the amplitude of the primary and secondary sphere and the sum of the total reflections detected, a generalized weld pool shape can be inferred as a function of time. At the start of the laser pulse, the majority of reflections exit the primary sphere and are captured by the secondary sphere. These high initial reflections not only show low absorption of laser power (825 W of the 1575 W is reflected) but, since they are mostly measured by the secondary sphere, the reflections are essentially parallel to the incoming beam. This implies a flat, largely perpendicular surface such as that expected at the onset of weld pool formation (Refs. 9–11). Once sufficient melting is reached, surface tension forms a semi-hemispherical weld pool reflecting light in all directions above the surface of the sample. This is evident by the rapid decrease in reflected light detected by the secondary sphere (red curve) and increasing reflection captured in the primary sphere (green curve). Over the next few milliseconds, laser power absorbed by the weld increases as the total measured reflections decrease (blue curve). The decrease in reflections is believed to be indicative of the formation of a weld pool keyhole and the rate of decrease is a measure of the rate at which the keyhole develops. Upon keyhole maturation at approximately 3–4 ms, reflections reach a minimum and are roughly constant

for the duration of the pulse. Laser power reflected at this point is ~25% of the power delivered. The metallographic section for this weld displays an aspect ratio common for keyhole mode welds of this depth — Fig. 8B. A weld pore is also present, identified by the dark elliptical region to the right of the weld's centerline.

The difference between the delivered power and the measured reflected power is the power absorbed to form the weld. This difference, or the absorbed power, is presented in Fig. 9A (blue curve) for a square pulse and Fig. 9B for a constant ramp down pulse, at 1575 W peak and 6 and 8 ms, respectively. The black curve is the laser pulse profile that was acquired prior to welding. [Ideally, the pulse profile and weld measurement would be made simultaneously; however, given the low pulse-to-pulse variation of this laser system (less than 3% determined by the Ophir meter), error incurred by independent measurements was determined to be acceptable.] At any point along the plot of power absorbed vs. time, power transfer efficiency (or instantaneous energy transfer) is calculated as the quotient of laser power absorbed over (blue curve) the laser power delivered (black curve). This numeric value, as already demonstrated, describes the state of the weld pool. At the onset of welding for both the square and CRD pulse, power transfer efficiency was <50%. As a keyhole developed with the high constant output power of the square pulse, efficiency rose to 75%. As output power was steadily decreased in the CRD pulse, a mature keyhole never formed and, in turn, transfer efficiency remains low at ~50%. The total transfer of laser energy quantified by the energy transfer efficiency is calculated as the quotient of energy absorbed (area under the weld curve) to the energy delivered (area under the pulse

profile curve). Energy transfer efficiency for the square pulse weld was 66% (6.3/9.5 J) and only 51% (3.25/6.35 J) for the CRD pulse. For the two pulse shapes defined, a range of parameters from 2 to 8 ms and 1.5–13 J was evaluated. Due to the large spot size of the 150-mm lens, keyhole mode welds with a CRD pulse shape were not formed.

To evaluate variations within this measurement technique, replicate welds were performed. Presented in Fig. 10 are three welds of 1575 W. Again, a keyhole mode weld is apparent due to the rapid rise in the transfer of laser power starting below 50% and increasing to a peak of 74%. As the three curves overlap, it may be inferred that interactions between the laser beam and the weld material are generally similar for the three welds, and despite the chaotic nature of weld pool dynamics commonly associated with keyhole mode welds (Refs. 7, 10–12), the overall rate of formation and general shape of the keyhole are very similar for each weld resulting in essentially equal energy transfer. The measured energy transfer efficiencies for the three welds in Fig. 9 were 60, 61, and 60%. The repeatability and consistent amplitude of the absorption measurements imply that small changes or instabilities within the keyhole have no appreciable effect on the total energy absorbed; and thus reducing complexities often incorporated in many thermal fluid weld models. Conduction and keyhole mode welds at 500 and 1000 W were also evaluated and showed similar repeatability. Constant ramp down pulse welds of 3 J at 4 and 6 ms were comparably repeatable.

Through Fresnel reflections (Refs. 13, 14), as the keyhole wall becomes more inclined (steeper), the decreased angle of incidence increases the number of reflec-

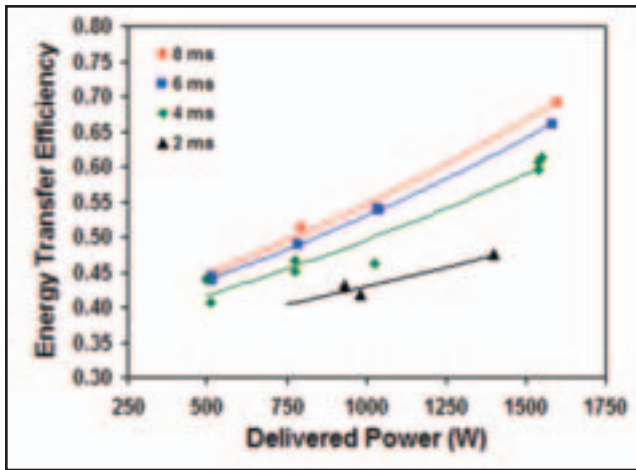


Fig. 13 — Energy transfer efficiency identified to increase with increasing pulse time and/or pulse duration.

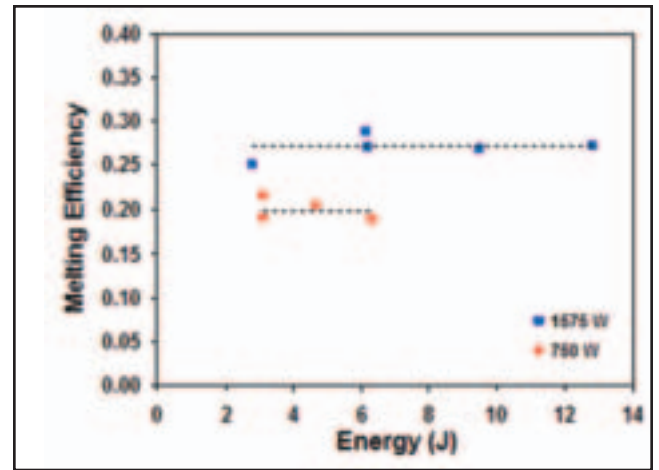


Fig. 14 — Melting efficiency is constant with power irrespective of pulse energy. Pulse time ranges from 2 to 8 ms. Both square and CRD pulses used.

tions (inside the keyhole) yielding a higher net transfer of laser energy. With each reflection, energy is both absorbed and reflected and with the decreased incident beam angle, more energy is deposited at the root of the keyhole. This drives high-aspect-ratio, high-efficiency welds. In Fig. 11A, three temporal absorption profiles of 500, 1033, and 1575 W are evaluated with pulse time constant at 6 ms. At 500 W (green curve), a relatively constant absorption profile is seen from weld start to finish yielding power transfer and energy efficiencies of ~47%. As expected, the metallographic cross section (Fig. 11B) reveals a low-aspect-ratio, conduction-mode weld. With increasing delivered power to 1033 W (red curve), a keyhole is formed as implied by the increased power absorption. Power transfer efficiency starts below 50% and increases to 65% yielding a total energy transfer efficiency of 54%. As previously discussed in Fig. 9, raising output power to 1575 W (blue curve, Fig. 11) yields, upon keyhole maturation, an even higher power transfer efficiency of 77% for an overall energy efficiency of 66%. Comparison of the 1033- and 1575-W welds shows the rate of keyhole maturation (time to maximum power transfer) to be nearly equivalent after ~4 ms. The constant power transfer from 4 to 6 ms implies a fully developed and quasi-stable keyhole. Although both welds are identified as keyhole mode welds, the peak power transfer efficiency at 1585 W is greater than that at 1033 W. The low peak power transfer of the 1033-W weld would imply a shallower keyhole with fewer internal reflections and thus a lower transfer efficiency. In support of this interpretation, the corresponding metallographic sections (Fig. 11B) show a lower weld aspect ratio for the 1033-W weld. Logically, the high-aspect-ratio 1575-W weld implies

that upon keyhole maturation, a deeper, more steeply inclined keyhole was formed resulting in the higher maximum power transfer value.

Also evident by comparison of the temporal absorption profiles presented in Fig. 11 is the dependence of overall energy transfer efficiency on the amplitude and rate of change of the power transfer. The fractional time at low and high power transfer rates, as well as the transitional time between, governs the overall energy transfer. This is more evident in Fig. 12 where four welds all having a delivered power of ~1575 W are evaluated at 2-, 4-, 6-, and 8-ms pulse times. The absorption profile (Fig. 12A) for each weld overlaps as pulse time increases. At 2 ms, there is insufficient time for keyhole development resulting in a low-transfer-efficiency weld with power and energy transfer less than 50%. As pulse time increases (from 4 to 8 ms), the relative amount of time spent in keyhole mode increases, thereby yielding a greater overall energy transfer. A peak power transfer of ~77% is reached and is again relatively constant after ~4 ms. At 4-, 6-, and 8 ms, energy transfer efficiency increases from 61% to 66% to 70%, respectively. Evaluation of the metallographic cross sections (Fig. 12B) reveals the progression of the weld as pulse time, energy, and efficiency increase. Each weld is similar in overall shape, with weld size increasing with pulse energy. After 4 ms, a single pore of common size is seen (root-type pores such as these are common in keyhole mode laser welds and are generally formed by the collapse of the weld pool keyhole (Ref. 10)).

As the amplitude and fraction of time in keyhole mode dictates the transfer of energy, greater energy efficiency is reached by increasing either pulse time or delivered power. In Fig. 13, energy trans-

fer efficiency is shown as a function of delivered power (or average power in the case of a CRD pulse) and pulse time. Here, both square and constant ramp down pulse shapes are included displaying a clear trend in energy transfer efficiency. At a low output power (i.e., 500 W), transfer efficiency increases from 41 to 45% by increasing time from 4 to 8 ms. At high output powers (i.e., 1575 W) over the same times, efficiency increases from 60 to 70%. It is clear that increasing power yields greater efficiency. In contrast, however, if pulse time is too short, inhibiting keyhole formation (i.e., 2 ms, black curve Fig. 13), only moderate increases in efficiency can be expected regardless of increasing output power. These measurements in energy transfer efficiency for milli-scale stainless steel welds are comparable to those presented by Fuerschbach and Cremers (Refs. 1, 4).

Also crucial for process optimization of laser beam spot welds is the characterization of melting efficiency (Ref. 15). As energy is transferred from the laser beam to the weld sample, heating and melting occur. For a given volume of material, the rate of heat input must be sufficient to induce melting. Melting efficiency is calculated as the weld volume ( $V$ ) times the heat of fusion ( $\delta h$ ) divided by the heat input ( $Q_{in}$ -energy absorbed) (Ref. 15).

$$\eta_m = \frac{V\delta h}{Q_{in}}$$

For a given quantity of heat, more melting is generated by increasing the rate of heat input since losses due to thermal diffusion through the base metal are minimized. This behavior is seen in Fig. 14 where melting efficiency is plotted as a

function of pulse energy. Regardless of pulse energy, melting efficiency was found to be a function of the delivered power, or the rate of heat input. In this plot, a latent heat of fusion for 304L steel of 8.7 J/mm<sup>3</sup> (Ref. 16) was used in the calculation. Data for power levels of 750 and 1575 W are shown, with pulse time varying from 2 to 8 ms. At 750 W, approximately 20% of the transferred energy results in melting. By increasing the rate of heat input to 1575 W, melting efficiency increases further to approximately 27%. Under 3D heat flow conditions, theoretical melting efficiency is maximum at 31% (Refs. 1, 17). Melting efficiency is further evaluated in Fig. 15 for delivered powers having both square and constant ramp down pulse shapes. Test parameters revealed melting efficiency to linearly increase with average power and to be independent of temporal pulse shape. By optimizing melting efficiency, both heat input and the weld's heat-affected zone are minimized.

## Conclusions

The presented method for quantifying energy absorption, which measures reflected laser light off the weld's surface, provides a temporal measure of the change in absorption as the state of the weld pool changes. The energy absorption measured by this method showed good agreement with calorimetric (Refs. 1, 2) and thermal expansion methods (Ref. 4). Analysis of this method is continuing, but the current results support the use of this method for energy absorption measurements in LBSWs. Specific conclusions are as follows:

1. Power transfer of < 50% is measured at the start of a laser pulse, but can increase to 80% given sufficient energy density and time to fully develop a keyhole.

2. The overall energy transfer depends upon the fractional time spent at high and low levels of power transfer efficiency.

3. Energy absorption was found to be invariant for replicate welds despite the dynamic nature of keyhole mode welding, thus reducing the complexities incorporated in many thermal fluid weld models, and providing empirically measured boundary conditions as a function of time for critical processing parameters.

4. Melting efficiency of a spot weld was found to be a function of pulse power for both square and constant ramp down pulse shapes.

Future research incorporating this measurement technique will evaluate changes in transfer and melting efficiencies resulting from dissimilar and high reflectivity materials (4047 Al to 6061 Al), and the effects of variable part fitup such as root opening and out-of-plane surfaces. Pulse shaping and the effect of gas shield-

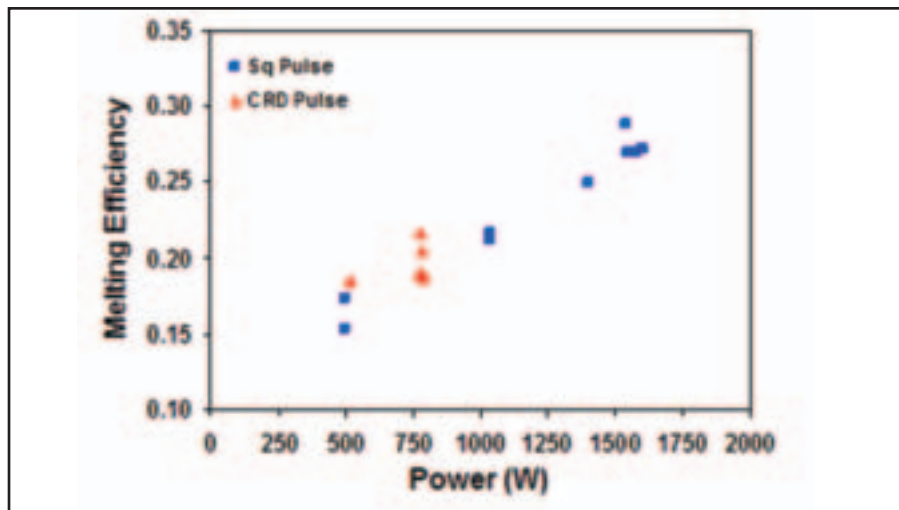


Fig. 15 — Melting efficiency mapped for various delivered powers and pulse shapes. Pulse time ranges from 2 to 8 ms.

ing are also of interest, as both have shown to be beneficial for optimal weld penetration efficiency and avoiding weld porosity (Ref. 18).

### Acknowledgments

The authors would like to thank A. Kilgo for her careful preparation of the metallographic samples, and Don Susan and Danny MacCallum for their thorough review of this manuscript. This work was performed at Sandia National Laboratories, which is a multiprogram laboratory operated by Sandia Corp., a Lockheed Martin Co., for the United States Department of Energy under contract DE-AC04-94AL85000.

### References

1. Fuerschbach, P. W., and Eisler, G. R. 2002. Effect of laser spot weld energy and duration on melting absorption. *STWJ* 7(4): 241–246.
2. Perret, O., Naudy, P., and Bizouard, M. 1999. Keyhole formation study in pulsed Nd:YAG laser welding. *ICALEO Proceedings*, Vol. 87 Sec. D, pp. 177–186.
3. Jouvard, J. M., Girard, K., and Perret, O. 2001. Keyhole formation and power deposition in ND:YAG laser spot welding. *J. Phys D: Appl. Phys.* Vol. 34: 2894–2901.
4. Cremers, D. A., Lewis, G. K., and Korzekwa, D. R. 1991. Measurement of energy deposition during pulsed laser welding. *Welding Journal* 70(7): 159-s to 176-s.
5. Hsien-Chee, L. 2005. *Introduction to Color Imaging Science*. Cambridge University Press: pp. 42–44.
6. DeWitt, D. P., and Nutter, G. D. 1988. *Theory and Practice of Radiation Thermometry*. Wiley-IEEE: pp. 143–150.
7. Jellison, J. L. 1991. Fundamentals of Metal Joining with Lasers. *Sandia National Laboratories Reports: #SAND91-0032C*.
8. Fuerschbach, P. W., Norris, J. T., Dykhuizen, R. C., and Mahoney, A. R. 2004.

Development and evaluation of an in-situ beam measurement for spot welding lasers. *Welding Journal* 83(5): 154-s to 159-s.

9. Katayama, S., Kohsaka, S., Mizutani, M., Nishizawa, K., and Matsunawa, A. 1993. Pulse shape optimization for defect prevention in pulsed laser welding of stainless steels. *ICALEO Proceedings* Vol. 77: 487–497.

10. Heiple, C. R., and Burgardt, P. 2005. Fluid flow phenomena during welding. *ASM Handbook* Vol. 6: 19–24. Materials Park, Ohio: ASM International.

11. Fujinaga, S., Takenaka, H., Narikiyo, T., Katayama, S., and Matsunawa, A. 2000. Direct observation of keyhole behavior during pulse modulated high-power Nd:YAG laser irradiation. *J. Phys. D: Appl. Phys.* Vol. 33: 492–497.

12. Mizutani, M., Katayama, S., and Matsunawa, A. 2003. Observation of molten metal behavior during laser irradiation — Basic experiment to understand laser welding phenomena. *SPIE Proceedings*, Vol. 4831: 208–213.

13. Jouvard, J. M., Perret, O., and Naudy, Ph. 2001. Keyhole formation and power deposit law in Nd:YAG laser welding. *SPIE Proceedings* Vol. 4184: 615–618.

14. Solana, P., and Guillermo, N. 1997. A study of the effect of multiple reflections on the shape of the keyhole in the laser processing of materials. *J. Phys. D: Appl. Phys.* Vol. 30: 3216–3222.

15. Fuerschbach, P. W. 1996. Measurement and prediction of energy transfer efficiency in laser beam welding. *Welding Journal* 75(1): 24-s to 34-s.

16. Leibowitz, L. 1976. Properties for LMFBR safety analysis. *Argonne National Labs: ANL-CEN-RSD-76-1*.

17. Rykalin, N. N. 1951. *Calculation of Heat Flow in Welding*. Translated by Zvi Paley and C. M. Adams Jr., Moscow.

18. Norris, J. T., Perricone, M. J., Roach, R. A., Faraone, K., and Ellison, C. 2007. Evaluation of weld porosity in laser beam seam welds: Optimizing continuous wave and square wave modulated processes. *ICALEO Proceedings: Paper No. 804*.